

1. Please check your article carefully, coordinate with any co-authors and enter all final edits clearly in the eproof, remembering to save frequently. If edits are needed to figures, please attach a corrected figure file containing the relevant changes. Once corrections are submitted, we cannot routinely make further changes to the article.

2. Note that the eproof should be amended in only one browser window at any one time; otherwise changes will be overwritten.

3. Author surnames have been highlighted. Please check these carefully and adjust if the first name or surname is marked up incorrectly, as this will affect indexing of your article in public repositories such as PubMed. Also, carefully check the spelling and numbering of all author names and affiliations, and the corresponding author(s) email address(es). Please note that email addresses should only be included for designated corresponding authors, and you cannot change corresponding authors at this stage except to correct errors made during typesetting.

4. You cannot alter accepted Supplementary Information files except for critical changes to scientific content. If you do resupply any files, please also provide a brief (but complete) list of changes. If these are not considered scientific changes, any altered Supplementary files will not be used, only the originally accepted version will be published.

5. If applicable, please ensure that any accession codes and datasets whose DOIs or other identifiers are mentioned in the paper are scheduled for public release as soon as possible, we recommend within a few days of submitting your proof, and update the database record with publication details from this article once available.

6. If ref. 57 (preprint) has now been published in final peer-reviewed form, please update the reference details if appropriate.

Article

Dissecting intervalley coupling mechanisms in monolayer transition metal dichalcogenides

Open Access This article is licensed under a Creative Commons Attribution-NonCommercial-NoDerivatives 4.0 International License, which permits any non-commercial use, sharing, distribution and reproduction in any medium or format, as long as you give appropriate credit to the original author(s) and the source, provide a link to the Creative Commons licence, and indicate if you modified the licensed material. You do not have permission under this licence to share adapted material derived from this article or parts of it. The images or other third party material in this article are included in the article's Creative Commons licence, unless indicated otherwise in a credit line to the material. If material is not included in the article's Creative Commons licence and your intended use is not permitted by statutory regulation or exceeds the permitted use, you will need to obtain permission directly from the copyright holder. To view a copy of this licence, visit <http://creativecommons.org/licenses/by-nc-nd/4.0/>.

Oleg Dogadov✉

Email : oleg.dogadov@polimi.it

Affiliationids : Aff1, Correspondingaffiliationid : Aff1

Henry Mittenzwey Affiliationids : Aff2

Micol Bertolotti Affiliationids : Aff1

Nicholas Olsen Affiliationids : Aff3

Thomas Deckert Affiliationids : Aff4

Chiara Trovatiello Affiliationids : Aff1 Aff5

Xiaoyang Zhu Affiliationids : Aff3

Daniele Brida Affiliationids : Aff4

Giulio Cerullo Affiliationids : Aff1 Aff6

Andreas Knorr Affiliationids : Aff2

Stefano Dal Conte✉

Email : stefano.dalconte@polimi.it

Affiliationids : Aff1, Correspondingaffiliationid : Aff1

Aff1 Department of Physics, Politecnico di Milano, Pi, Milan, Italy

Aff2 Institut für Theoretische Physik, Nichtlineare Optik und Quantenelektronik, Technische Universität Berlin, Berlin, Germany

Received: 21 July 2025 / Accepted: 10 December 2025

Abstract

Monolayer (1L) transition metal dichalcogenides (TMDs) provide a unique opportunity to control the valley degree of freedom of optically excited charge carriers due to the spin-valley locking effect. However, a unified picture of competing intervalley coupling processes in 1L-TMDs is lacking. Here, we apply broadband helicity-resolved transient absorption to explore exciton valley polarization dynamics in 1L-WSe₂. By combining experimental results with microscopic simulations, we dissect individual intervalley coupling mechanisms and reveal the crucial role of phonon-assisted scattering in the fast decay of the A exciton circular dichroism and the formation of the dichroism of opposite polarity for the B exciton. We further provide a consistent description of the valley depolarization driven by an intervalley-exchange-activating momentum-dark Dexter process and indicate the presence of efficient single electron spin-flip mechanisms. Our study advances understanding of exciton dynamics in TMDs.

Introduction

The presence of two energy degenerate valleys with opposite orbital magnetic moments and Berry curvatures in monolayer (1L) group VI transition metal dichalcogenides (TMDs) has stimulated a wide interest in the study of the valley-contrasting physics in these materials[1,2,3,4,5]. The particular interest for this class of compounds is explained by their outstanding optical properties. In addition to the presence of the two non-equivalent valleys at K and Γ points of the Brillouin zone, the reduced dimensionality of 1L-TMDs, their direct gap, and a large spin-orbit interaction give rise to tightly bound exciton states[6], which can be selectively addressed in K and Γ valleys with light of opposite helicity[7,8,9]. However, for a successful use of the valley degree of freedom in prospective devices[3,4], a way to generate and control a robust valley polarization, i.e., population difference of the two valleys, must be achieved. An understanding of the microscopic processes governing the intra- and intervalley dynamics in 1L-TMDs after optical excitation becomes therefore a critical factor. **AQ1 AQ2 AQ3 AQ4 AQ5**

Ultrafast optical spectroscopies provide powerful methods to study exciton dynamics in 1L-TMDs[10]. Transient Faraday or Kerr rotation spectroscopy[11,12] and helicity-resolved pump-probe (also referred to as transient circular dichroism (CD)) spectroscopy[13,14,15] are the two widely used techniques that allow one to address the dynamics of valley degrees of freedom. These studies have revealed an ultrafast coupling of the valleys in 1L-TMDs[16], which has been attributed to different many-body correlations[13,17,18]. Intervalley electron-hole exchange interaction based on Coulomb-interaction-induced energy transfer has been initially proposed to explain the fast loss of valley polarization[19,20,21]. However, phonon-assisted intervalley electron scattering has also been suggested to be an efficient process in 1L-TMDs[12,22,23,24,25,26,27,28]. Moreover, a Dexter-like intervalley interaction based on Coulomb-interaction-induced charge transfer that mixes the A and B excitonic transitions from opposite valleys might also contribute to the valley depolarization process[18,29], whereas a coupling of A and B excitons in the same valley can be induced by intravalley exchange[30]. The spin-valley physics becomes particularly complicated for the case of spin-dark materials, such as WSe₂ or WS₂, where the role of different mechanisms is still debated[23,31,32,33]. Although many of the above mentioned interaction mechanisms have been studied before on their own, it is still unclear how their combined action affects the valley (de-)polarization dynamics in 1L-TMDs and whether there is a predominant mechanism.

In this work, we apply broadband femtosecond transient CD spectroscopy to study the spin-valley relaxation dynamics in 1L-WSe₂. By simultaneously characterizing the A and B excitons, we are able to resolve complex dynamics of the two transitions, and unveil the presence of multiple inter- and intravalley relaxation channels. We simulate the valley-resolved exciton dynamics by solving the microscopic Heisenberg equations of motion for coherent transitions and incoherent occupations within a unit operator method[34,35]. We find that initial decay of the A exciton CD signal and the formation of the B exciton CD of the opposite sign are mainly due to a fast intervalley phonon-assisted scattering, while the valley depolarization on a longer timescale is governed by an exchange-activating momentum-dark Dexter interaction, which has not yet been described in the literature. A strong temperature dependence of the CD dynamics suggests an unequal equilibration of electrons and holes, due to an additional electron single spin-flip mechanism. Thanks to the excellent agreement of numerical simulations and experimental results, our combined study is able to evaluate the role of multiple excitonic interaction processes governing the spin-valley dynamics in 1L-TMDs.

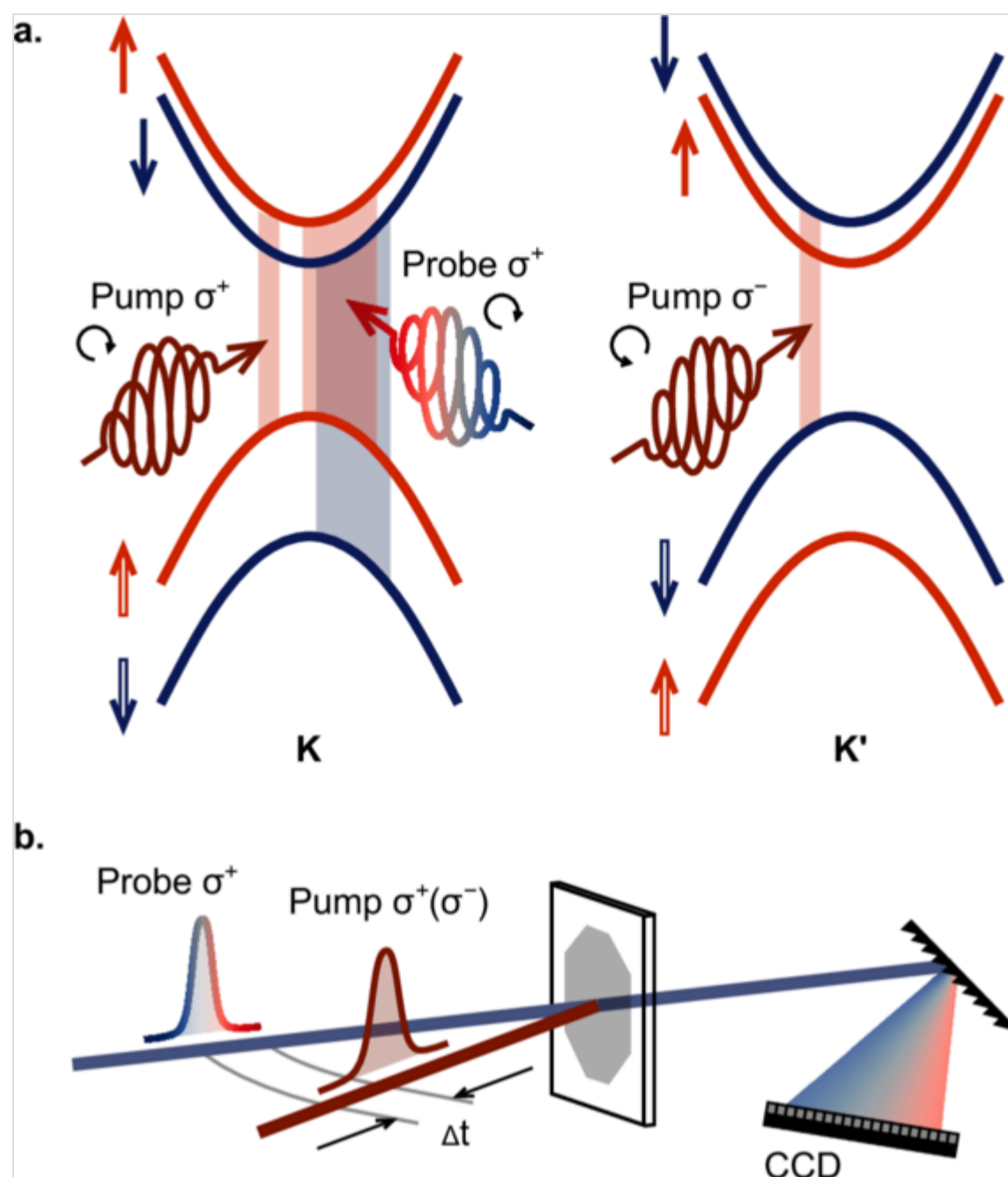
Results

Experiment

Experiments are performed on a large-area 1L-WSe₂ on SiO₂ substrate, fabricated with gold-assisted mechanical exfoliation technique (see Methods section for details). We use femtosecond differential transmission (DT) spectroscopy with circularly polarized pulses to access intra- and intervalley dynamics. We resonantly excite the A exciton 1s state with either right (σ^+) or left (σ^-) circularly polarized pulses to selectively generate A excitons in either K or Γ valley. The ~ 25 meV energy width of the pump pulses limits the temporal resolution of our experiments to ~ 100 fs, as confirmed by measuring the instrumental response function (IRF). A broadband σ^+ -polarized supercontinuum probe tracks the dynamics of the A and B excitons in the K valley. Figure 1 illustrates the principle and implementation of the experiment. The CD is calculated as the difference of the two DT signals following excitation with opposite helicities:

Here, $\Delta T/T := (T_{\text{pump on}} - T_{\text{pump off}})/T_{\text{pump off}}$, where $T_{\text{pump on}}$ and $T_{\text{pump off}}$ are transmission signals with and without pump, respectively. The double indices in Equation (1) specify the pump (first) and the probe (second) polarizations.

a Valence and conduction band spin splitting in K and K' points of the Brillouin zone of 1L-WSe₂, giving rise to A and B excitons. Color coding shows bands with the same spin orientation, indicated with solid arrows for electrons and double arrows for holes. Right (σ^+) and left (σ^-) circularly polarized pulses couple to two nonequivalent valleys of a 1L-TMD. Broadband σ^+ probe covers both A and B excitons at the K point. **b** Diagram of a transient CD experiment.



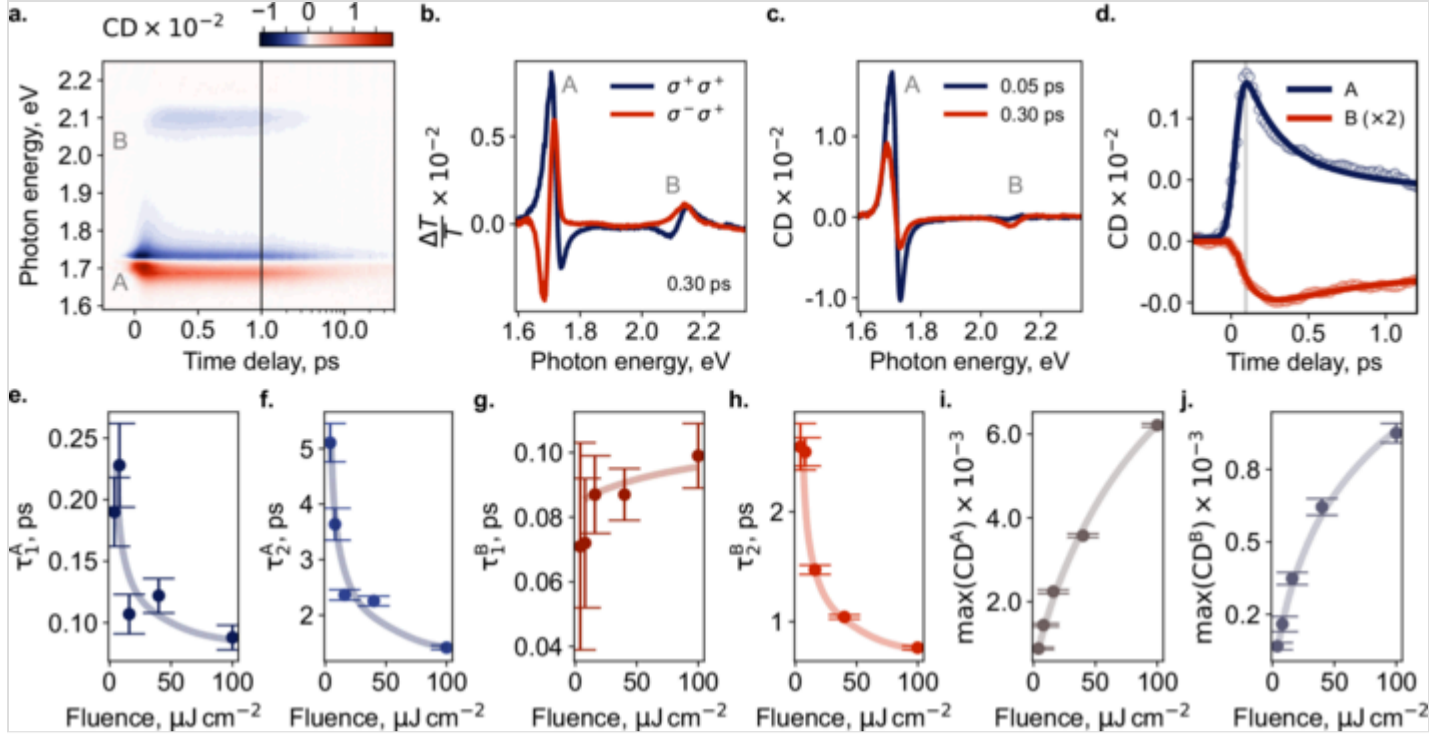
Transient circular dichroism

Figure 2a reports transient CD data at 77 K, as a function of probe photon energy E and pump-probe delay Δt . The CD signal is calculated from the two DT maps measured for opposite pump helicities, as defined in Eq. (1). In this measurement, the sample is excited in resonance with the A exciton with $8 \mu\text{J cm}^{-2}$ fluence, which corresponds to $\sim 8 \times 10^{11} \text{ cm}^{-2}$ photocarrier density. The map reveals the presence of complex transient signals around A and B exciton resonances, i.e., 1.7 eV and 2.1 eV, respectively. The A exciton CD signal shows a dispersive line shape, changing its sign from positive to negative, as the probe photon energy increases. The B exciton signal, instead, is dominated by a negative component. The origin of the CD signal is illustrated in Fig. 2b and c. Panel (b) depicts DT spectra at 0.30 ps time delay for two pump helicities (σ^+/σ^-) resonant with the A exciton and broadband σ^+ probe. Both A and B exciton resonances have different line shapes and signal strengths, giving rise to distinct CD signals. Transient CD spectra in Fig. 2c, obtained from the map (a) at two time delays, show that the rapid decrease of the A exciton CD signal within first 0.30 ps upon photoexcitation is accompanied by a delayed formation of a B exciton CD signal.

Fig. 2

Valley-resolved dynamics.

a Pseudo-color energy-time CD pump-probe map, as defined in Eq. (1), $8 \mu\text{J cm}^{-2}$ pump fluence. **b** Transient spectra at 0.3 ps for two pump circular polarizations. **c** Transient spectra of the CD map (a) at select time delays. **d** Spectrally averaged temporal CD traces of A and B excitons. Vertical line shows the time delay of maximum A exciton CD magnitude. Dots correspond to experimental points, solid lines show the fit. **e–j** Fluence dependence. **e**, **f** Fluence dependence of the two lifetime components for A exciton. **g**, **h** Same for B exciton. **i**, **j** Fluence dependence of magnitudes of A and B CD signals, respectively. Solid lines in (e–j) are guides to eye. All measurements are performed at 77 K.



The transient CD signal thus has a complex shape, originating from valley population imbalance and many-body effects[17,36,37]. To isolate the temporal evolution of the degree of valley polarization we perform a spectral integration of the CD signal over 300 meV energy ranges around the exciton peaks. Spectrally averaged A and B exciton transient CD traces are shown in Fig. 2d, which isolates the Pauli-blocking-induced bleaching dynamics. The graph reveals opposite signs of the A and B excitons' CD signals, as previously observed in 1L-WS₂[15,18]. Furthermore, whereas the signal of A exciton is formed within the pump pulse duration, the B exciton CD has a finite formation time, as shown with a vertical line, marking the time delay at which the trace of the A exciton reaches its maximum value. The traces are fitted with a biexponential function, convoluted with a single Gaussian profile, which represents the IRF of the system:

2

Here, H is a Heaviside step function, C is a constant offset. We find that the fast relaxation component of the A exciton signal τ_1 fs and the formation signal of the B exciton CD τ_2 fs are of the same order, suggesting that common processes govern their dynamics. The slower relaxation times of both signals are found to be on a picosecond timescale with a faster decay of the B exciton signal. Figure 2e-j reports a pump fluence dependence of the first ("short") and the second ("long") time constants for the CD signals of the two excitons, as well as the maximum values of the CD. The magnitudes of the signals show a sub-linear scaling with pump fluence, which is related to the saturation of the DT signals for both pump helicities[38,39]. As the pump fluence increases, the depolarization dynamics, characterized by the second time constants τ_2 , extracted for the CD signals of both excitons becomes faster, as shown in Fig. 2f and h. Such behavior was previously observed in different 1L-TMDs[40,41] and it was explained by an enhanced exciton-exciton exchange interaction at increased carrier densities[41]. We comment on the possible origin of this effect in the Discussion section. Importantly, for all investigated fluences the decay time of the B exciton CD signal is shorter than that of the A exciton. We also find that as the pump fluence increases, the first time constant τ_1 becomes shorter for the A exciton, whereas for the B exciton it remains unchanged within the precision of our measurements. The higher uncertainty in the definition of τ_1 is due to the fact that its value is on the same order as the duration of the pump pulse. We note that even for the highest applied pump fluence the photocarrier density is approximately an order of magnitude lower than the expected Mott transition threshold[42,43].

To confirm the main observations reported above, we perform two-color time-resolved Faraday rotation measurements. In these experiments, the dynamics of the valley population imbalance is measured by the photoinduced rotation of the linearly-polarized probe polarization, originating from the different refractive indexes experienced by its σ^+ and σ^- components[40,44]. The performed measurements support our observations, demonstrating the opposite sign of the valley polarization for A and B excitons, as well as the shorter depolarization time for the B exciton. The outline of the experimental setup and the experimental results are presented in Supplementary Notes 2 and 14, respectively.

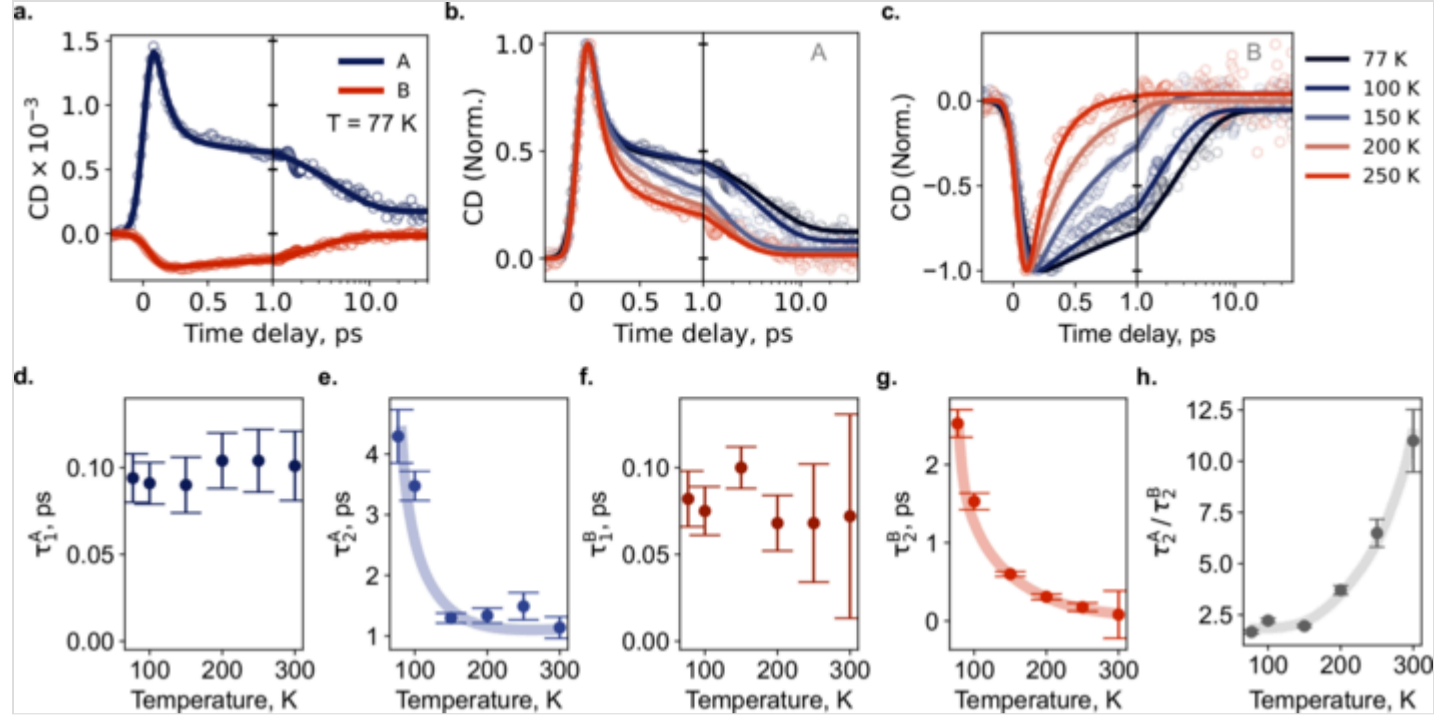
Temperature dependence

We further explore the temperature dependence of the CD signal, following resonant excitation of the A exciton with $8 \mu\text{J cm}^{-2}$ pump fluence. Figure 3a compares CD traces of A and B excitons at 77 K. The temperature dependencies of the CD signals of A and B excitons are separately presented in panels (b, c), respectively. While the fast depolarization component of the A exciton CD and the formation time of the B exciton CD are weakly affected by temperature, the long decay time for both A and B excitons becomes progressively shorter as the temperature increases. The results of the lifetime analysis of the CD signals approximated with the function in Equation (2) are summarized in Fig. 3d-h.

Fig. 3

Temperature dependence.

a Spectrally averaged CD signals of A and B excitons at 77 K. b, c Temperature dependence of A and B exciton CD signals, respectively. In a-c, dots are experimental points, and solid lines show a biexponential fit. d-h Temperature dependence of the time constants τ_1 (d) and τ_2 (e) for CD signal of A exciton, τ_1 (f) and τ_2 (g) for CD signal of B exciton, and the ratio of the second lifetime components τ_2/τ_1 for two excitons (h). Solid lines in e, g, h are guides to eye.



The increase of the depolarization rate for A exciton at higher temperatures shown in Fig. 3e is in agreement with the previously reported studies for 1L-TMDs [11, 40, 41], in which it has been explained by the Coulomb exchange interaction [41] or phonon-mediated intervalley spin-flip transitions [23]. In our measurements, a similar effect is also observed for the B exciton CD (Fig. 3g). However, the temperature effect on the depolarization dynamics of the B exciton is more prominent. Figure 3h shows how the ratio of the depolarization times for A and B excitons changes with temperature. Within the accuracy of the lifetime analysis, the ratio remains unchanged up to ca. 150 K. As the temperature increases further, the depolarization rate of the B exciton CD accelerates faster than that of the A exciton, and at 300 K, its depolarization time is an order of magnitude shorter. Such anomalous temperature dependence of the B exciton polarization suggests that, apart from the above mentioned processes, an additional temperature dependent spin-flip mechanism must be considered to correctly describe this effect. Note that, while the lifetime of the B exciton CD signal experiences such strong temperature dependence, the $\Delta T/T$ signal itself does not show a significant temperature dependence of the relaxation time (see Supplementary Note 15).

Theoretical model

The experimentally observed opposite sign of the CD signals for A and B excitons suggests the presence of strong intervalley coupling mechanisms. As mentioned before, coherent interactions related to the pump-induced excitonic polarization are expected to play an important role in the spin-valley dynamics of 1L-TMDs. However, the fact that the B exciton CD signal shows a finite formation time implies the presence of efficient incoherent mechanisms, which involve excitonic populations in the two valleys. For a comprehensive description of the spin-valley dynamics it is crucial therefore to consider the combined action of different interaction mechanisms.

To obtain an in-depth explanation of the experimentally observed CD signatures and to disentangle the role of phonon-assisted intervalley scattering and Coulomb intervalley coupling processes, we perform microscopic simulations for the exciton dynamics. The calculation scheme for the temporal evolution of the coherent excitonic polarization P (see Eqs. (4) and (9) in the Methods), and the incoherent exciton occupation N (see Eqs. (8) and (10) in the Methods), is based on a Heisenberg equations of motion approach in a correlation expansion of electron-hole pairs (see Supplementary Note 3) [34, 35, 45].

Before delving into the theoretical model in detail, we first establish the optical observable to create a one-to-one correspondence to the measured signals. Since the aim of this work is to examine the physical mechanisms which determine the dynamics of the excitonic bleaching (Pauli-blocking) signal (see for instance Fig. 2d) we disregard all coherent pump-induced spectral signatures due to Coulomb interaction such as excitation-induced energy renormalization and broadening [37, 46, 47, 48] or excitation-induced broadening due to exciton-phonon interaction [49]. Upon energy-averaging the experimentally measured DT spectra around the respective excitonic resonances, the influence of these excitation-induced spectral signatures on the probed signal vanishes and only Pauli-blocking due to pump-induced coherent and incoherent excitonic occupations remains. Therefore, the energy-averaged DT signal $\Delta T(E^i, \Delta t)$ around excitonic energy E^i for $i = A, B$ dependent on the pump-probe delay Δt by using Eq. (6) can be expressed as [50]:

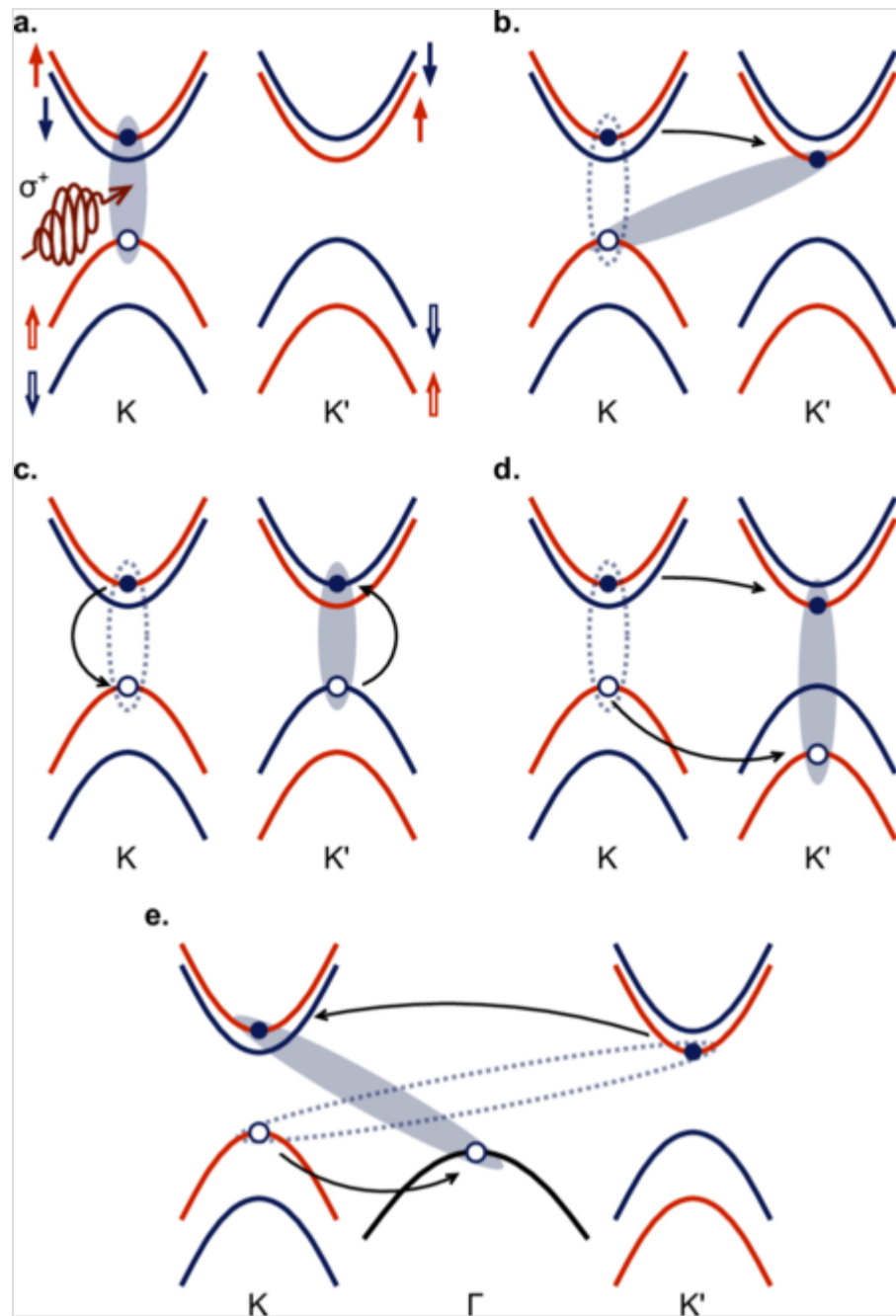
3

In Eq. (3), i denotes the probed transition and \cdot (A and B exciton) denotes the respective coherent (\cdot) at $\mathbf{Q} = \mathbf{0}$ or incoherent (\cdot) excitonic occupation with respect to the center-of-mass momentum \mathbf{Q} contributing to the Pauli-blocking mediated by the bleaching form factors \cdot . These factors are given in Eq. (7) of the Methods and consistently take into account the fermionic substructure of the exciton via encoding Pauli-blocking by the individual holes and electrons. Therefore, the DT signal depends on the oscillator strength of the probed excitonic transition i , as well as on the occurrence of electron and/or hole Pauli-blocking due to excitonic occupations in the state \cdot , as soon as the electron and/or the hole of the pump-induced excitonic occupation overlap with any electron and/or hole of the probed transition in the state i . This is illustrated exemplarily in Fig. 4a and b: After the optical pump in Fig. 4a, bleaching of the B transition at \cdot occurs. From Eq. (3), the simulated CD signal is obtained using Eq. (1). In the following, we discuss the CD dynamics in terms of the bleaching-inducing momentum-integrated occupations N . However, in our simulations we always take into account the full momentum-dependent overlap between the bleaching form factors $D_{\mathbf{Q}}$ (defined in Eq. (7) in Methods) and the excitonic occupations $N_{\mathbf{Q}}$.

Fig. 4

Select intervalley exciton occupation scattering processes in 1L-WSe₂ in K and L valleys.

We show the processes that follow σ^+ excitation, creating A excitons in K valley, as shown in (a). Solid and double colored arrows indicate electron and hole spin states, respectively. (b) Intervalley phonon-assisted electron scattering. (c) Resonant intervalley exchange. Incoherent Dexter interaction on intravalley (d) and intervalley (e) occupations. Dashed ellipses illustrate initial exciton states, filled ellipses show final exciton states.



Having established the relation of the coherent exciton polarization P and occupations N_Q to the measured spectra, we turn to the microscopic model. Sketches in Fig. 4 illustrate the possible exciton intervalley scattering processes after σ^+ excitation of the A exciton at the K point (Fig. 4a), which might occur in the following and primarily contribute to the dynamics of the CD signals of A and B excitons. In our calculations, we take into account phonon-assisted incoherent exciton formation and thermalization, as well as intervalley scattering [28, 51] (panel (b)), Coulomb-mediated intervalley exchange scattering (Förster coupling, double spin flips) [19, 20, 52] (panel (c)), and Coulomb-mediated direct intervalley scattering of intra- and intervalley excitonic occupations (Dexter coupling) [18, 29] (panels (d) and (e), respectively). We also examine the role of the coherent Dexter-like intervalley exciton coupling, which instantaneously mixes A and B excitons in opposite valleys [18]. Details to all matrix elements and equations of motion can be found in the Supplementary Notes 4–7.

Figure 5 compares the measured and simulated CD signals at 77 K (a) and 250 K (b). For both the temperatures, a good agreement between the experiment and the theory is obtained. The simulations accurately capture the initial fast decay of the A exciton signal and the delayed formation of the B exciton CD, as well as the relative strengths of dichroism signals of A and B excitons. Moreover, the overall decay of the CD signal, which is experimentally shown to be faster at higher temperatures, is correctly reproduced in the simulations. Our calculations, however, do not reproduce the faster decay of the B exciton CD signal compared to that of the A exciton.

Fig. 5

Experimental and simulated results.

Comparison of normalized A and B exciton CD traces for 77 K (a) and 250 K (b).

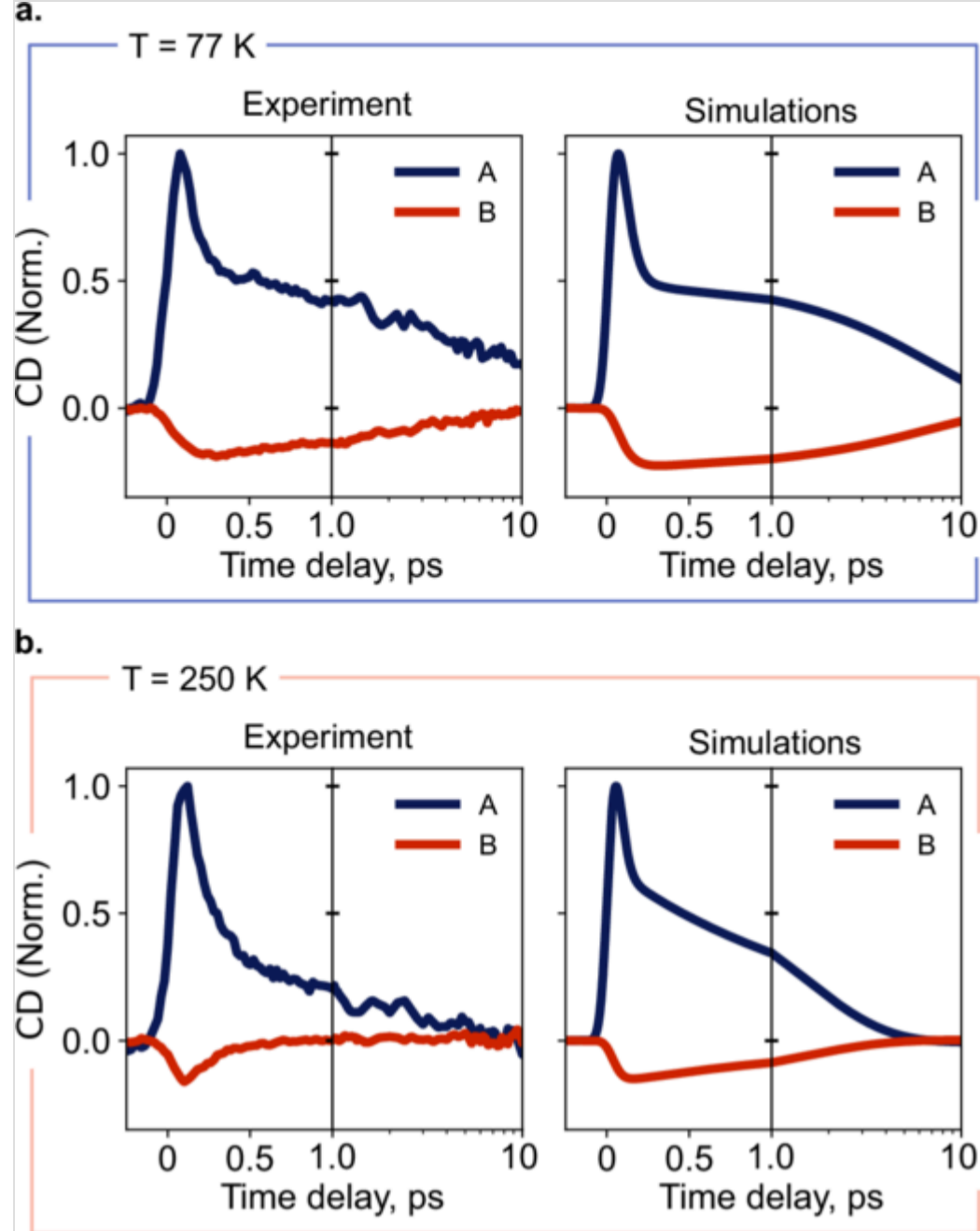
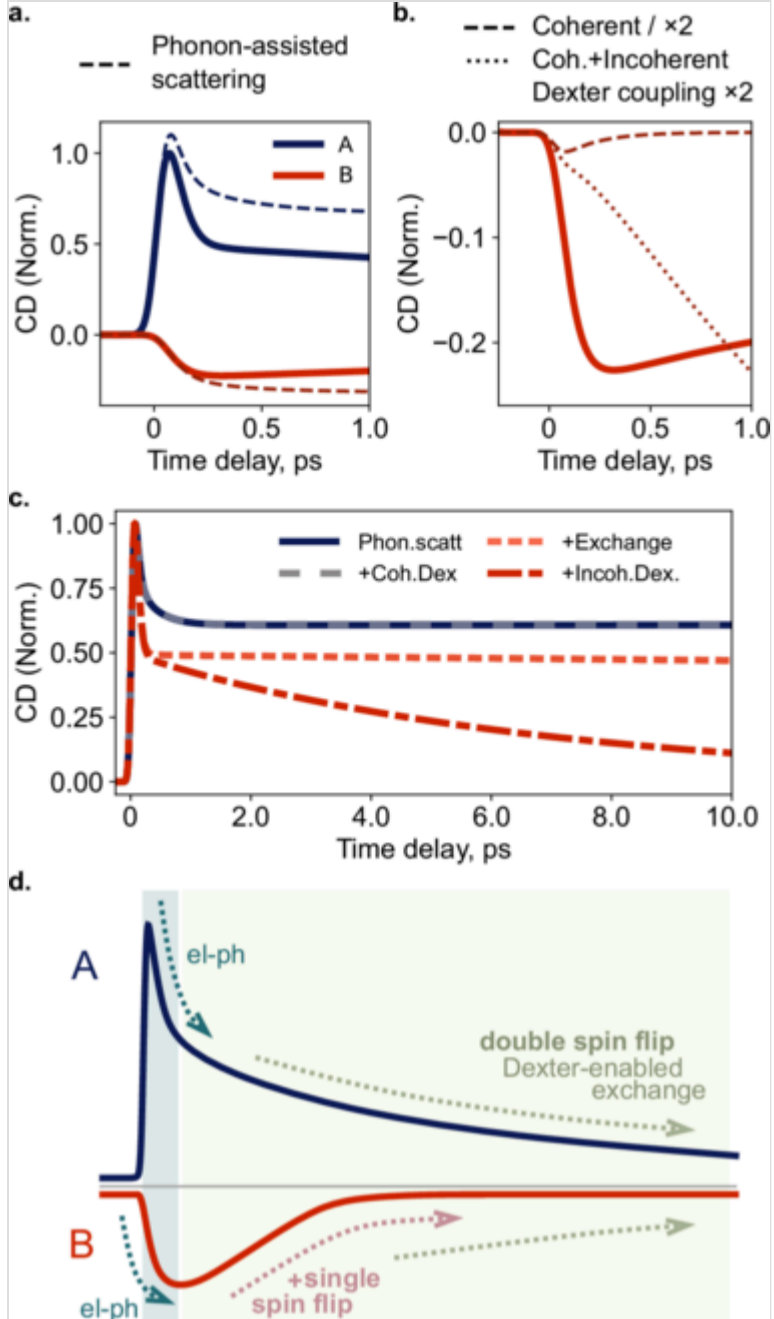


Figure 6 shows in detail the modeled CD dynamics along with individual contributions of selected coupling mechanisms. In the next section, we present an in-depth discussion of the role of different physical processes and provide an explanation to the main experimental observables.

Fig. 6

Contribution of select processes to the CD signal at 77 K.

a Comparison of total simulated CD traces with the phonon-assisted intervalley scattering contribution to the CD. **b** Total simulated B exciton CD compared to the effect of Dexter coupling (coherent and incoherent) alone. The Dexter coupling traces are magnified by a factor of 2 for clarity. In both panels, the traces are normalized to the maximum A exciton CD value (for complete simulations). **c** Contributions of phonon-assisted scattering, coherent Dexter coupling, intervalley exchange, and incoherent intervalley Dexter coupling to the overall decay of the A exciton CD signal. **d** Summary of the main processes. A cartoon schematically shows the CD dynamics of A and B excitons in 1L-WSe₂ and highlights the key processes, governing the dynamics. See details in text.



Discussion

Upon pumping the A exciton transition in the K valley shown in Fig. 4a and a subsequent phonon-assisted dephasing of coherent excitonic polarizations into incoherent excitonic intravalley occupations, spin-preserving phonon-assisted intervalley scattering leads to the formation of energetically lower intervalley occupations $K_{\uparrow\downarrow}$ occupations (in this notation, the first (second) index denotes the valley spin of the hole \uparrow, \downarrow (electron \uparrow, \downarrow) of the corresponding exciton), as shown in Fig. 4b. This process occurs mainly via the spontaneous emission of phonons, which explains the relative insensitivity of the fast decay of the A exciton CD to temperature (see Fig. 3b). In the simulations, we also include scattering to intermediate states at the Λ valleys (not shown in Fig. 4), which causes an overall speed-up of the phonon-assisted intervalley scattering. Overall, the CD signal of the probed A transition is positive, since intervalley $K_{\uparrow\downarrow}$ occupations cause a bleaching in the $\sigma^+\sigma^+$ pump-probe configuration at the K valley due to the hole remaining there, whereas intervalley $-K_{\downarrow}$ occupations induce no bleaching in the $\sigma^-\sigma^+$ pump-probe configuration, because the hole is located at the \downarrow valley and the electron at the K valley has an opposite spin compared to the probed transition, see Equation (1). The probed B transition, instead, experiences a bleaching in the $\sigma^-\sigma^+$ configuration due to the electron part of the intervalley $-K_{\downarrow}$ excitonic occupation, whereas the bleaching of the probed B signal in the $\sigma^+\sigma^+$ configuration is zero, since $K_{\uparrow\downarrow}$ occupations do not contribute to the Pauli-blocking in the probed B transition at the K valley (see Fig. 4b). This explains the experimentally observed negative CD signal, see Eq. (1).

In Fig. 6a, the formation of the A and B CD signals is depicted for the full simulations (solid lines) and when only phonon-assisted scattering processes are taken into account (dashed lines). Since these traces are qualitatively similar for both A and B excitons, we conclude that phonon-assisted spin-preserving intervalley scattering of electrons is the most relevant mechanism of the initial decay of the A exciton CD signal and the delayed formation of the B exciton CD of opposite polarity (see also the results of calculations at 250 K in Supplementary Fig. 13).

Importantly, according to our calculations, coherent Dexter coupling [18] cannot explain the observed behavior: Although due to this mechanism the B excitonic transition in the \downarrow valley is instantaneously excited when the A exciton at the K valley is resonantly optically pumped, this process is by more than an order of magnitude too inefficient to generate the CD signal for the B exciton in Fig. 6b. Due to the large energetic mismatch of A and B excitons, the off-resonantly Dexter-excited B excitonic polarization just follows the optically excited A exciton polarization adiabatically and almost no dephasing of coherent B excitonic polarization into incoherent B excitonic population occurs. We also find that the incoherent Dexter coupling (illustrated in Fig. 4d), which involves excitonic populations instead of polarizations, causes a delayed build-up of the B signal, which is stronger than that obtained by considering the coherent one only. However, the combination of coherent and incoherent Dexter coupling results in a CD signal which is too small and with a too long rise time to explain the measured CD dynamics, as shown in Fig. 6b.

Now, we discuss the overall decay of the CD signals, i.e., the valley depolarization dynamics. In contrast to the initial fast decay of the A signal and the delayed formation of the B signal, the overall decay of both CD signals cannot be explained by phonon-assisted scattering alone, and additional spin flip processes need to be taken into account. Figure 6c depicts the impact of different exciton scattering processes on the valley depolarization dynamics of the A CD signal. Since only double-spin-flip processes are included in our simulations (the total spin of electron and hole is conserved during all the considered scattering mechanisms), the effect of the discussed processes on the B exciton CD decay, within our calculations, is identical. We note that, due to the above mentioned large energetic mismatch between A and B excitons, the coherent Dexter interaction does not give any sizable loss of the A exciton CD signal, as seen in Fig. 6c.

Although the intervalley exchange is a double spin-flip process, as shown in Fig. 4c, it does not lead to a valley depolarization on its own due to its suppression when momentum-dark intervalley occupations (shown in Fig. 4b) dominate [53], in contrast to the case of spin-bright materials, such as 1L-MoSe₂ [19]. It becomes therefore necessary to destabilize the energetically favorable intervalley occupation.

According to our calculations, the most significant impact on the valley depolarization is provided by the additional incoherent momentum-dark Dexter interaction on intervalley occupations, shown in Fig. 4e, which is a different mechanism compared to the Dexter interaction between intravalley polarizations and occupations [18, 29, 54]. Although it does not cause a valley depolarization on its own, since it conserves the spin, momentum-dark intervalley Dexter coupling (Fig. 4e) leads to an activation of double-spin-flip-inducing intervalley exchange (Fig. 4c) by breaking the quasi-stable configuration of intervalley excitons: A fraction of the excitons is constantly upconverted into $\Gamma - K_{\uparrow}$ -excitons in a first step, which then feed into $K_{\uparrow} - K_{\downarrow}$ -excitons via phonon-assisted hole scattering, where intervalley exchange subsequently acts upon. This complex interplay then leads to an overall temperature-dependent decay of both CD signals, which excellently reproduces the measured decay of the A signal. A detailed explanation of the depolarization mechanism can be found in the Supplementary Note 13. To the best of our knowledge, the momentum-dark Dexter interaction has not yet been explored in literature, despite its major importance. We also note that since the valley depolarization results from the complex interplay of several processes, we expect that at higher fluences additional contributions, which are quadratic in the excitonic occupations $\propto N^2$ or higher, will contribute to all processes considered, which would explain the observed acceleration of the depolarization dynamics, reported in Fig. 2e and f. However, to the best of our knowledge, no density-dependent excitonic theory, which combines phonon-assisted scattering [49] and Coulomb intra- and interband scattering, exists so far.

We note that our model does not capture the experimentally observed faster decay of the B exciton CD signal compared to that of the A exciton. This difference in the CD decay dynamics implies that spin-down (spin-up) electrons at the K (Γ) valley, which govern the B exciton CD signal, equilibrate faster than the corresponding holes, which are monitored by the A exciton CD signal. This effect can possibly be due to the Rashba spin-orbit interaction, which induces single spin flips, as soon as an out-of-plane electric field is present in a sample [55, 56]. Due to the much larger valence band splitting compared to the conduction band splitting, spin hybridization of electrons is more likely compared to spin hybridization of holes. Thus, phonon-assisted spin flips between electrons are expected to be much faster than phonon-assisted scattering between holes [15]. Although several mechanisms that can potentially generate an out-of-plane electric field in 1L-TMDs have been proposed (including image charges at dielectric boundaries [57, 58], local strain [59], non-thermal [60] or chiral [61, 62, 63] phonons), the evaluation of the applicability of these mechanisms to our system of interest is beyond the scope of the present work. Figure 6d summarizes the discussion. A and B exciton signals show opposite valley polarization. The fast dynamics (light blue area), i.e., the rapid decay of the A exciton CD, as well as the delayed formation of the B exciton CD, is mainly defined by the efficient intervalley electron-phonon scattering (Fig. 4b). The long (depolarization) dynamics (light green area) results from a complex interplay of different processes. The overall loss of valley polarization is due to the Coulomb-mediated intervalley exchange, which is a double spin flip process (Fig. 4c). This process is enabled by the momentum-dark incoherent Dexter interaction acting on intervalley occupations (Fig. 4e). We further rationalize that additional phonon-assisted spin flips between electrons contribute to the faster decay of the B exciton CD signal.

In our work, we have focused on spin-valley dynamics in 1L-WSe₂. It is important to note, however, that the conclusions provided here are relevant also to other 1L-TMDs, and the developed theoretical approach can be applied to other systems. We argue that it is necessary to consider the discussed processes for a correct description of exciton dynamics in other spin-dark materials, such as 1L-WS₂. For the case of 1L-MoS₂, we expect the single spin flip for electrons to be even more efficient than in the studied case, due to the crossing of the spin-split conduction bands close to the K and Γ points of the Brillouin zone [64, 65]. Our results are also consistent with the current understanding of the valley dynamics in 1L-MoSe₂, which is a spin-bright material [66]: Since phonon-assisted intervalley electron scattering is energetically unfavorable, no intervalley exciton population is created, and therefore a very fast valley depolarization is observed within ca. 1 ps [33, 67] due to the intervalley exchange [19], which remains fully active through the course of time.

In conclusion, we have performed a combined experimental-theoretical study of intervalley coupling processes in 1L-WSe₂ and assessed their role in the spin-valley relaxation processes. By applying broadband transient CD spectroscopy we have revealed notable dichroism signals for both A and B excitons, implying the presence of strong intervalley coupling mechanisms. The opposite sign of the CD signals for A and B excitons, the initial fast decay of the A exciton CD signal and the delayed formation of the B exciton CD signal can be explained by intervalley phonon-assisted electron scattering. To correctly describe the decay of the CD signals, i.e., the overall valley depolarization dynamics, instead, one needs to consider additional effects: While intervalley exchange alone is not sufficient to explain the measured valley depolarization dynamics, the complex interplay of the exchange-activating momentum-dark Dexter interaction with phonon-assisted scattering provides a very good agreement of the simulations with the experimentally observed results. Additionally, we have found experimentally that the B exciton CD signal shows a much faster decay, compared to the A exciton one, indicating that the electron spin-valley imbalance gets equilibrated faster than that of holes. Prospective studies comprise a detailed investigation of possible mechanisms for single-spin processes in 1L-TMDs.

Methods

Experimental set-up

Time-resolved measurements are performed in transmission geometry (see Supplementary Fig. 1). The same setup with different detection schemes is used for the transient CD and for the TRFR measurements. The setup is seeded by a regeneratively amplified Ti-sapphire laser (Coherent, Libra), which provides 100-fs pulses at 1.55 eV at a 2 kHz repetition rate. Narrowband pump pulses are generated in a home-built noncollinear optical parametric amplifier (NOPA), tuned to the energy of the A exciton 1s state (1.70 eV), and modulated by a mechanical chopper at half repetition rate of the amplifier (1 kHz). The broadband supercontinuum probe is generated by focusing 1.55 eV beam in a 2 mm-thick β -BaB₂O₄ plate. The spectral region below 1.59 eV is eliminated by a short-pass filter. The polarization states of pump and probe beams are controlled separately by a combination of linear polarizers and achromatic waveplates. The two beams are focused on a sample inside a cryostat (Oxford Instruments) at almost normal incidence with a small angle ($\sim 5^\circ$) between them. The transmitted circularly polarized probe is detected by a spectrometer with a silicon CCD. The time traces are acquired by scanning relative delays between pump and probe pulses by a motorized delay stage.

Sample preparation

Macroscopic 1L-WSe₂ is exfoliated via the gold tape exfoliation method[68]. Bulk WSe₂, grown via chemical vapor transport (CVT), have been purchased from HQ Graphene. Gold tape is prepared by evaporating gold onto a polished silicon wafer before spin coating a protective layer of polyvinylpyrrolidone (PVP). A 150 nm layer of gold is deposited onto the polished silicon wafer at a rate of 0.05 nm/s (Angstrom Engineering EvoVac Multi-Process thin film deposition system). A solution of PVP (40,000mw Alfa Aesar), ethanol, and acetonitrile with a 2:9:9 mass ratio is spun onto the gold surface of the wafer (1000 rpm, 1000 rpm/s acceleration, 2 min) before curing on a hot plate (150 °C, 5 min). Using thermal release tape (Semiconductor Equipment Corp. Revalpha RA-95LS(N)), the gold tape is removed from the silicon wafer and is pressed onto the surface of a bulk TMD crystal to exfoliate a large area monolayer. After placing the 1L-WSe₂ onto the final substrate, the sample assembly is heated on a hot plate at 130 °C to remove the thermal release tape. The sample assembly is soaked in deionized water for 3 h and in acetone for 1 hour to remove any remaining polymer residue. Then, the gold is then etched for 5 min in a KI/I₂ gold etchant solution (Iodine, 99.99%, Alfa Aesar; potassium iodide, 99.0%, Sigma-Aldrich, and deionized water with a 4:1:40 mass ratio). The sample is soaked in deionized water for 2 h, rinsed in isopropanol, and dried with N₂.

Theoretical calculations

The differential transmission signal is obtained by developing the excitonic Bloch equations for the excitonic transitions:

by taking into account the light-matter interaction within a correlation expansion in electron-hole pairs in the excitonic picture[35,45] up to the third order in the optical field \mathbf{E} . The excitonic transition operator is defined by:

where μ is the excitonic quantum number, \mathbf{Q} is the center-of-mass momentum, the index pairs \cdot and \cdot denote the valley and spin of the hole (first index) and electron (second index) forming the corresponding exciton. We denote the spins of the hole as $s = \uparrow, \downarrow$ and the spins of the electron as \cdot . Moreover, \mathbf{q} is the relative momentum, \cdot is the excitonic wave function solving the Wannier equation, α, β are the effective-mass ratios of the corresponding exciton and $v^\dagger(\mathbf{c})$ is the valence band electron creation (conduction band electron annihilation) operator. The equations of motion for the probe-induced excitonic transitions \cdot read:

where \cdot is the excitonic energy, \cdot is the excitonic non-radiative dephasing, \cdot is the total optical probe field with incoming field \cdot (delta-shaped probe pulse with pump-probe delay time Δt) and macroscopic polarization \mathbf{P}^{pr} and $\mathbf{d}^{cv,\zeta,s}$ is the interband transition dipole moment[69]. \cdot are the bleaching form factors, given by:

where the first contribution is related to Pauli-blocking by holes and the second is related to Pauli-blocking by electrons of the corresponding coherently excited pump-induced exciton occupation, and pump-induced incoherent excitonic occupation \cdot :

The equations of motion for the pump-induced excitonic transitions read:

and the equations of motion for the pump-induced excitonic occupations read:

The individual free “0” and optical “op” contributions are given in Supplementary Note 4, the exciton-phonon contributions “X-phon” are given in Supplementary Note 5, the Coulomb exchange contributions “Coul,X” are given in Supplementary Note 6, and the Coulomb Dexter contributions “Coul,Dex” are given in Supplementary Note 7. From the probe-induced transition in Eq. (6), the macroscopic probe-induced polarization \cdot can be established, which enables the calculation of the transmission by self-consistently solving Maxwell’s Equations[70,71]. The differential transmission ΔT is then obtained by subtracting the transmission of the probe pulse without the pump pulse from the transmission of the probe pulse with the pump pulse, yielding Equation (3) in the main part of the manuscript.

Supplementary information

The online version contains supplementary material available at <https://doi.org/10.1038/s41699-025-00653-2>.

Publisher’s note Springer Nature remains neutral with regard to jurisdictional claims in published maps and institutional affiliations.

Acknowledgements

N.O. acknowledges the assistance of Anthony Calderon and Alex Smirnov in sample preparation. O.D. and G.C. acknowledge financial support from European Union’s NextGenerationEU Investment 1.1, PRIN 2022 PNRR HAPPY [ID P20224AWLB, CUP D53D23016720001]. S.D.C. and G.C. acknowledge financial support by the European Union’s NextGenerationEU Programme with the I-PHOQS Infrastructure [IR0000016, ID D2B8D520, CUP B53C22001750006] “Integrated infrastructure initiative in Photonic and Quantum Sciences.” S.D.C. acknowledges support from the European Union’s NextGenerationEU – Investment 1.1, M4C2 - Project n. 2022LA3TJ8 – CUP D53D23002280006. Fabrication of macroscopic monolayer samples was supported as part of Programmable Quantum Materials, an Energy Frontier Research Center funded by the U.S. Department of Energy (DOE), Office of Science, Basic Energy Sciences (BES), under award DE-SC0019443. H.M. and A.K. acknowledge financial support from the Deutsche Forschungsgemeinschaft (DFG) through Project KN 427/11-2, Project No. 420760124. A.K. acknowledges financial support from the DFG through Project KN 427/15-1, Project No. 556436549. D.B. and T.D. acknowledge support from the FEDER Project LuxUltrafast 2 2023-01-04. C.T. acknowledges the European Union’s Horizon Europe research and innovation program under the Marie Skłodowska-Curie PIONEER HORIZON-MSCA-2021-PF-GF grant agreement No 101066108.

Author contributions

O.D. and S.D.C. devised the experiment; O.D. and M.B. conducted the experiment; O.D., M.B., and T.D. analyzed the data; H.M. performed the theoretical work; N.O. and C.T. fabricated and characterized the sample; O.D. and H.M. wrote the manuscript with input from all coauthors; X.Y.Z., D.B., A.K., G.C., and S.D.C. oversaw the project.

Data availability

All data needed to evaluate the conclusions in the paper are present in the main text and the Supplementary Materials. Raw data will be available in an

Competing interests

The authors declare no competing interests.

Supplementary information

Supplementary information

References

1. Xiao, D., Liu, G. B., Feng, W., Xu, X. & Yao, W. Coupled spin and valley physics in monolayers of MoS₂ and other group-VI dichalcogenides. *Phy. Rev. Lett.* **108**, 196802 (2012).
2. Xu, X., Yao, W., Xiao, D. & Heinz, T. F. Spin and pseudospins in layered transition metal dichalcogenides. *Nat. Phys.* **10**, 343–350 (2014).
3. Schaibley, J. R. et al. Valleytronics in 2D materials. *Nat. Rev. Mater.* **1**, 16055 (2016).
4. Liu, Y. et al. Valleytronics in transition metal dichalcogenides materials. *Nano Res.* **12**, 2695–2711 (2019).
5. Siwen, Z. et al. Valley manipulation in monolayer transition metal dichalcogenides and their hybrid systems: status and challenges. *Rep. Prog. Phys.* **84**, 026401 (2021).
6. Chernikov, A. et al. Exciton binding energy and nonhydrogenic rydberg series in monolayer WS₂. *Phys. Rev. Lett.* **113**, 076802 (2014).
7. Sallen, G. et al. Robust optical emission polarization in MoS₂ monolayers through selective valley excitation. *Phys. Rev. B* **86**, 081301 (2012).
8. Zeng, H., Dai, J., Yao, W., Xiao, D. & Cui, X. Valley polarization in MoS₂ monolayers by optical pumping. *Nat. Nanotechnol.* **7**, 490–493 (2012).
9. Mak, K. F., Xiao, D. & Shan, J. Light–valley interactions in 2D semiconductors. *Nat. Photonics* **12**, 451–460 (2018).
10. Dal Conte, S., Trovatiello, C., Gadermaier, C. & Cerullo, G. Ultrafast photophysics of 2D semiconductors and related heterostructures. *Trends Chem.* **2**, 28–42 (2020).
11. Zhu, C. R. et al. Exciton valley dynamics probed by Kerr rotation in WSe₂ monolayers. *Phys. Rev. B* **90**, 161302 (2014).
12. Plechinger, G. et al. Valley dynamics of excitons in monolayer dichalcogenides. *Phys. Status Solidi (RRL) - Rapid Res. Lett.* **11**, 1700131 (2017).
13. Mai, C. et al. Many-body effects in valleytronics: direct measurement of valley lifetimes in single-layer MoS₂. *Nano Lett.* **14**, 202–206 (2014).
14. Mai, C. et al. Exciton valley relaxation in a single layer of WS₂ measured by ultrafast spectroscopy. *Phys. Rev. B* **90**, 041414 (2014).
15. Wang, Z. et al. Intravalley spin-flip relaxation dynamics in single-layer WS₂. *Nano Lett.* **18**, 6882–6891 (2018).
16. Lloyd, L. T. et al. Sub-10 fs intervalley exciton coupling in monolayer mos2 revealed by helicity-resolved two-dimensional electronic spectroscopy. *ACS Nano* **15**, 10253–10263 (2021).
17. Schmidt, R. et al. Ultrafast coulomb-induced intervalley coupling in atomically thin WS₂. *Nano Lett.* **16**, 2945–2950 (2016).
18. Berghäuser, G. et al. Inverted valley polarization in optically excited transition metal dichalcogenides. *Nat. Commun.* **9**, 971 (2018).
19. Selig, M. et al. Ultrafast dynamics in monolayer transition metal dichalcogenides: interplay of dark excitons, phonons, and intervalley exchange. *Phys. Rev. Res.* **1**, 022007 (2019).
20. Yu, T. & Wu, M. Valley depolarization due to intervalley and intravalley electron-hole exchange interactions in monolayer MoS₂. *Phys. Rev. B* **89**, 205303 (2014).
21. Combescot, M., Amand, T. & Shiao, S.-Y. Ab initio quantum approach to electron-hole exchange for semiconductors hosting Wannier excitons. *Phys. Rev. B* **107**, 115206 (2023).
22. Kioseoglou, G., Hanbicki, A. T., Currie, M., Friedman, A. L. & Jonker, B. T. Optical polarization and intervalley scattering in single layers of MoS₂ and MoSe₂. *Sci. Rep.* **6**, 25041 (2016).

23. Molina-Sánchez, A., Sangalli, D., Wirtz, L. & Marini, A. Ab initio calculations of ultrashort carrier dynamics in two-dimensional materials: valley depolarization in single-layer WSe₂. *Nano Lett.* **17**, 4549–4555 (2017).
24. Carvalho, B. R. et al. Intervalley scattering by acoustic phonons in two-dimensional MoS₂ revealed by double-resonance Raman spectroscopy. *Nat. Commun.* **8**, 14670 (2017).
25. Brem, S. et al. Phonon-assisted photoluminescence from indirect excitons in monolayers of transition-metal dichalcogenides. *Nano Lett.* **20**, 2849–2856 (2020).
26. He, M. et al. Valley phonons and exciton complexes in a monolayer semiconductor. *Nat. Commun.* **11**, 618 (2020).
27. Bae, S. et al. K-point longitudinal acoustic phonons are responsible for ultrafast intervalley scattering in monolayer MoSe₂. *Nat. Commun.* **13**, 4279 (2022).
28. Selig, M. et al. Dark and bright exciton formation, thermalization, and photoluminescence in monolayer transition metal dichalcogenides. *2D Mater.* **5**, 035017 (2018).
29. Bernal-Villamil, I. et al. Exciton broadening and band renormalization due to Dexter-like intervalley coupling. *2D Mater.* **5**, 025011 (2018).
30. Guo, L. et al. Exchange-driven intravalley mixing of excitons in monolayer transition metal dichalcogenides. *Nat. Phys.* **15**, 228–232 (2019).
31. Huang, J., Hoang, T. B., Ming, T., Kong, J. & Mikkelsen, M. H. Temporal and spatial valley dynamics in two-dimensional semiconductors probed via Kerr rotation. *Phys. Rev. B* **95**, 075428 (2017).
32. Koutensky, P. et al. Ultrafast dynamics of valley-polarized excitons in WSe₂ monolayer studied by few-cycle laser pulses. *Nanomaterials* **13**, 1207 (2023).
33. Raiber, S. et al. Ultrafast pseudospin quantum beats in multilayer WSe₂ and MoSe₂. *Nat. Commun.* **13**, 4997 (2022).
34. Ivanov, A. L. & Haug, H. Self-consistent theory of the biexciton optical nonlinearity. *Phys. Rev. B* **48**, 1490–1504 (1993).
35. Katsch, F., Selig, M., Carmele, A. & Knorr, A. Theory of exciton-exciton interactions in monolayer transition metal dichalcogenides. *Phys. Status Solidi* **255**, 1800185 (2018).
36. Sie, E. J., Frenzel, A. J., Lee, Y.-H., Kong, J. & Gedik, N. Intervalley biexcitons and many-body effects in monolayer MoS₂. *Phys. Rev. B* **92**, 125417 (2015).
37. Deckert, T. et al. Coherent coulomb intra- and intervalley many-body effects in single-layer transition metal dichalcogenides. *Phys. Rev. Lett.* **135**, 066902 (2025).
38. Kumar, N. et al. Exciton-exciton annihilation in MoSe₂ monolayers. *Phys. Rev. B* **89**, 125427 (2014).
39. Seo, M. et al. Ultrafast optical microscopy of single monolayer molybdenum disulfide flakes. *Sci. Rep.* **6**, 21601 (2016).
40. Dal Conte, S. et al. Ultrafast valley relaxation dynamics in monolayer MoS₂ probed by nonequilibrium optical techniques. *Phys. Rev. B* **92**, 235425 (2015).
41. Mahmood, F., Alpichshev, Z., Lee, Y.-H., Kong, J. & Gedik, N. Observation of exciton-exciton interaction mediated valley depolarization in monolayer MoSe₂. *Nano Lett.* **18**, 223–228 (2018).
42. Chernikov, A., Ruppert, C., Hill, H. M., Rigosi, A. F. & Heinz, T. F. Population inversion and giant bandgap renormalization in atomically thin WS₂ layers. *Nat. Photonics* **9**, 466–470 (2015).
43. Dendzik, M. et al. Observation of an excitonic Mott transition through ultrafast core-cum-conduction photoemission spectroscopy. *Phys. Rev. Lett.* **125**, 096401 (2020).
44. Hsu, W.-T. et al. Optically initialized robust valley-polarized holes in monolayer WSe₂. *Nat. Commun.* **6**, 8963 (2015).
45. Fricke, J. Transport equations including many-particle correlations for an arbitrary quantum system: a general formalism. *Ann. Phys.* **252**, 479–498 (1996).
46. Katsch, F., Selig, M. & Knorr, A. Exciton-scattering-induced dephasing in two-dimensional semiconductors. *Phys. Rev. Lett.* **124**, 257402 (2020).

47. Trovatiello, C. et al. Disentangling many-body effects in the coherent optical response of 2D semiconductors. *Nano Lett.* **22**, 5322–5329 (2022).
48. Katsch, F., Selig, M. & Knorr, A. Theory of coherent pump–probe spectroscopy in monolayer transition metal dichalcogenides. *2D Mater.* **7**, 015021 (2019).
49. Katzer, M. et al. Exciton-phonon scattering: competition between the bosonic and fermionic nature of bound electron-hole pairs. *Phys. Rev. B* **108**, L121102 (2023).
50. Policht, V. R. et al. Time-domain observation of interlayer exciton formation and thermalization in a MoSe₂/WSe₂ heterostructure. *Nat. Commun.* **14**, 7273 (2023).
51. Thränhardt, A., Kuckenburg, S., Knorr, A., Meier, T. & Koch, S. Quantum theory of phonon-assisted exciton formation and luminescence in semiconductor quantum wells. *Phys. Rev. B* **62**, 2706 (2000).
52. Maialle, M. Z., e Silva, E.dA. & Sham, L. Exciton spin dynamics in quantum wells. *Phys. Rev. B* **47**, 15776 (1993).
53. Selig, M. et al. Suppression of intervalley exchange coupling in the presence of momentum-dark states in transition metal dichalcogenides. *Phys. Rev. Res.* **2**, 023322 (2020).
54. Jasiński, J. et al. Control of the valley polarization of monolayer wse2 by dexter-like coupling. *2D Mater.* **11**, 025007 (2024).
55. Winkler, R. *Spin-orbit Coupling Effects in Two-Dimensional Electron and Hole Systems* (Springer Berlin, 2003).
56. Mittenzwey, H. et al. Ultrafast optical control of rashba interactions in a TMDC heterostructure. *Phys. Rev. Lett.* **134**, 026901 (2025).
57. Mittenzwey, H. & Knorr, A. Many-body rashba spin-orbit interaction and exciton spin relaxation in atomically thin semiconductor structures. Preprint at <https://doi.org/10.48550/arXiv.2509.04285> (2025). **AQ6**
58. Slobodeniuk, A. & Basko, D. Spin–flip processes and radiative decay of dark intravalley excitons in transition metal dichalcogenide monolayers. *2D Mater.* **3**, 035009 (2016).
59. Zhuang, X., He, B., Javvaji, B. & Park, H. S. Intrinsic bending flexoelectric constants in two-dimensional materials. *Phys. Rev. B* **99**, 054105 (2019).
60. Schlipf, M. & Giustino, F. Dynamic rashba-dresselhaus effect. *Phys. Rev. Lett.* **127**, 237601 (2021).
61. Lagarde, D. et al. Efficient electron spin relaxation by chiral phonons in WSe₂ monolayers. *Phys. Rev. B* **110**, 195403 (2024).
62. Chan, Y. -h. et al. Exciton thermalization dynamics in monolayer MoS₂: a first-principles Boltzmann equation study. *Phys. Rev. B* **111**, 184305 (2025).
63. Zhang, X.-W. & Cao, T. Ab initio calculations of spin-nonconserving exciton–phonon scattering in monolayer transition metal dichalcogenides. *J. Phys. Condens. Matter* **34**, 264002 (2022).
64. Kormányos, A. et al. $k \cdot p$ theory for two-dimensional transition metal dichalcogenide semiconductors. *2D Mater.* **2**, 022001 (2015).
65. Liu, G.-B., Shan, W.-Y., Yao, Y., Yao, W. & Xiao, D. Three-band tight-binding model for monolayers of group-VIB transition metal dichalcogenides. *Phys. Rev. B* **88**, 085433 (2013).
66. Maja, F., Samuel, B., August, E. & Ermin, M. Brightening of spin- and momentum-dark excitons in transition metal dichalcogenides. *2D Mater.* **8**, 015013 (2020).
67. Jeong, T.-Y. et al. Valley depolarization in monolayer transition-metal dichalcogenides with zone-corner acoustic phonons. *Nanoscale* **12**, 22487–22494 (2020).
68. Liu, F. et al. Disassembling 2D van der Waals crystals into macroscopic monolayers and reassembling into artificial lattices. *Science* **367**, 903–906 (2020).
69. Mkrtchian, G. F., Knorr, A. & Selig, M. Theory of second-order excitonic nonlinearities in transition metal dichalcogenides. *Phys. Rev. B* **100**, 125401 (2019).

70. Knorr, A., Hughes, S., Stroucken, T. & Koch, S. Theory of ultrafast spatio-temporal dynamics in semiconductor heterostructures. *Chem. Phys.* **210**, 27–47 (1996).

71. Jahnke, F., Kira, M. & Koch, S. Linear and nonlinear optical properties of excitons in semiconductor quantum wells and microcavities. *Z. für Physik B Condens. Matter* **104**, 559–572 (1997).